The Journal of Chemical Physics

Semiglobal diabatic potential energy matrix for the N–H photodissociation of methylamine

Cite as: J. Chem. Phys. **152**, 244309 (2020); https://doi.org/10.1063/5.0008647
Submitted: 09 April 2020 . Accepted: 05 June 2020 . Published Online: 26 June 2020

Kelsey A. Parker, and Donald G. Truhlar

The Journal of Chemical Physics ARTICLE scitation.org/journal/jcp

Semiglobal diabatic potential energy matrix for the N–H photodissociation of methylamine

Cite as: J. Chem. Phys. 152, 244309 (2020); doi: 10.1063/5.0008647
Submitted: 9 April 2020 • Accepted: 5 June 2020 •
Published Online: 26 June 2020

Kelsey A. Parker and Donald G. Truhlar[a)]

AFFILIATIONS

Department of Chemistry, Chemical Theory Center, and Minnesota Supercomputing Institute, University of Minnesota, Minneapolis, Minnesota 55455-0431, USA

[a)]Author to whom correspondence should be addressed: truhlar@umn.edu

ABSTRACT

We constructed an analytic diabatic potential energy matrix (DPEM) that describes the N–H photodissociation of methylamine; the electronic state space includes the ground and first excited singlet states. The input for the fit was calculated by extended multi-state complete active space second-order perturbation theory. The data were diabatized using the dipole–quadrupole diabatization method in which we incorporated a coordinate-dependent weighting scheme for the contribution of the quadrupole moments. To make the resulting potential energy surfaces semiglobal, we extended the anchor points reactive potential method, a multiscale approach that assigns the internal coordinates to categories with different levels of computational treatment. Key aspects of the adiabatic potential energy surfaces obtained by diagonalizing the DPEM agree with the available experimental and theoretical data at energies relevant for photochemical studies.

I. INTRODUCTION

Upon photoexcitation with ultraviolet light, methylamine shows interesting dynamics that have been well studied but are not fully understood. The interesting photodynamics of methylamine coupled with its small size make it a good test system to improve our understanding of photochemical processes and to improve and test our computational methods for treating such systems. The first step in such a program of study is to obtain potential energy surfaces and their couplings, and this is the objective of the present paper.

Methylamine has been studied with many experimental and theoretical methods.[1–22] In 1963, Michael and Noyes detected dissociation reactions of methylamine after excitation to the first ultraviolet absorption band.[1] The dominant dissociation pathway was found to be N–H dissociation, but C–H and C–N dissociations were also detected. These reactions were also detected by Waschewsky and co-workers upon excitation at 222 nm in collisionless conditions.[2] Using Hartree–Fock calculations to study the ground and first excited singlet states (S_0 and S_1, respectively), Kassab *et al.* showed that S_1 corresponded to the excitation of a nitrogen lone pair electron to a 3s Rydberg orbital.[3] Along N–H and C–N dissociation coordinates, this orbital assumes a σ^* character, and conical intersections (CIs) between the ground and first excited states were found along both dissociation coordinates. Building on this work, Dunn and Morokuma studied S_0 and S_1 along N–H, C–N, and C–H dissociation coordinates.[4] Along the N–H and C–N slices, they found barriers at short distances and CIs at larger distances in good agreement with Kassab *et al.* Both studies also noted a change in the amino structure from pyramidal to planar upon excitation to S_1. More recent work by Xiao and co-workers[5] explored critical points on the two surfaces, and we will compare to their findings in Sec. III. We are most interested in studying the N–H dissociation, but we will show that our diabatization method is also capable of treating the C–N and C–H dissociations.

The potential energy surfaces of methylamine can help us to understand the system's interesting photodynamics. Ashfold and co-workers, using photofragment translational spectroscopy, studied the kinetic energy spectra of H photofragments, which they found to be bimodal.[6,7] They found that N–H dissociation dominates over

C–H dissociation, and they assigned the fast and slow components of the H photofragments to two pathways for N–H dissociation with both pathways leading to ground-electronic-state products and with both pathways involving H atoms initially tunneling through or passing over a barrier at short N–H distances on the excited surface. More recent work supports their conclusion about the dominance of N–H dissociation.[8–13]

Several studies have looked into how vibrational excitation affects photodissociation,[8–15,17] including vibrational mode effects on reaction yields,[8,9] lifetimes,[11] average photofragment translation energy,[14] and branching ratios.[13–15] Comparison of deuterated vs non-deuterated species gives strong evidence of tunneling, which likely plays a major role in fast passage through the N–H barrier on the excited surface.[11]

Very recently, Wang and co-workers[16] constructed a diabatic potential energy matrix (DPEM) for methylamine by fitting data at geometries obtained by sampling the coordinate space with trajectories. Our approach is different from them but shares some key features with the methods they used; in particular, we both use a diabatic representation and we both prioritize the regions of the DPEM, which are important for dynamics.

To generate data for our fitting procedure, we used extended multi-state complete active space second-order perturbation theory[23] (XMS-CASPT2), which improves upon MS-CASPT2[24] by introducing invariance[25] with respect to the rotation of the basis vectors in the model space. The XMS-CASPT2 calculations yield the energies of the two lowest singlet states in the adiabatic representation. In this representation, the energies (adiabatic potentials) are diagonal elements of the electronic Hamiltonian, and the states are coupled by the nuclear momentum and nuclear kinetic energy operators. For semiclassical calculations, one usually only deals with the vector couplings due to the nuclear momentum operator,[26,27] and these couplings are called nonadiabatic couplings or NACs.[28] When adiabatic states approach one another, which is ubiquitous in photochemistry, the adiabatic state functions change rapidly, and the adiabatic potentials become equivalent at conical intersection seams. These properties result in the adiabatic potentials having high-dimensional cuspidal ridges (called conical intersections or conical intersection seams) along nuclear coordinates and the NACs becoming large as the states approach and becoming singular along conical intersection seams.[28]

In a diabatic representation,[27–30] which is not unique, the NACs are negligible, and the electronic wave functions are smooth functions of the nuclear coordinates. The electronic Hamiltonian in a diabatic representation is nondiagonal and is called the diabatic potential energy matrix (DPEM); the elements of this matrix are the diabatic potentials on the diagonal and the diabatic couplings off the diagonal, and they are all smooth functions of nuclear coordinates.[28,31] For fitting purposes, a diabatic representation is preferable compared to the adiabatic representation because the diabatic potentials and diabatic couplings can be fit to analytical functions, and the NACs can be neglected. Therefore, we will fit the surface in a diabatic representation in the present work. We note that once a diabatic fit has been obtained, it is straightforward and inexpensive to transform into an equivalent adiabatic one.[32]

Therefore, before we fit the surfaces, we must convert the directly calculated adiabatic surfaces to a DPEM, which is called diabatization. Many diabatization methods have been developed, and for the present study, we used the dipole–quadrupole (DQ) diabatization method.[33,34] The DQ method makes use of the dipole moment and the quadrupole moment to distinguish the diabatic states. The quadrupole contribution has an origin dependence, and multiple quadrupole origins can be used. Furthermore, the contributions of the moments can be weighted, and in this study, we extend the applicability of the DQ diabatization method by introducing coordinate-dependent weights on the quadrupole contributions.

Analytical DPEMs and adiabatic potentials, which are obtained by diagonalizing the DPEM, are very useful for dynamics because they are very cost effective as compared to direct dynamics, and therefore, they allow more ensemble averaging and longer trajectories at an affordable cost. However, it is not necessary to fit a fully global DPEM that would be valid for all ranges of all internal coordinates. Rather, it is sufficient to produce a semiglobal DPEM that gives reasonable accuracy for dynamically accessed geometries in the photochemical process being studied. Methylamine has 15 degrees of freedom, and we treat 2 of them globally and the other 13 in restricted ranges of geometry. For this purpose, we use the anchor points reactive potential (APRP) method, which was originally developed for precisely this kind of semiglobal surface fitting.[35]

The APRP scheme involves distinguishing the internal coordinates of the system into primary, secondary, and tertiary coordinates, but in this work, we use only primary and tertiary coordinates. Along the primary coordinates, we fit the diabatic potentials to globally realistic functions valid even in the region of dissociated geometries. The dependence of the diabatic potentials on tertiary coordinates is treated by local fits centered at anchor points corresponding to fixed points in the primary coordinate space. The tertiary fits depend parametrically on the primary coordinates. Between the anchor points, tent functions of the primary coordinates interpolate the tertiary contribution.

In previous APRP studies,[35–38] the tertiary contribution was obtained by using Hessians calculated at the anchor points. In the present work, we instead calculated energies at finite displacements of the tertiary coordinates from the anchor points. We then fit the energies to analytic functions of the tertiary coordinates.

The present work involved a second modification of the previous anchor points procedure, in particular, with regard to the tent functions. In previous work, to interpolate between the anchor points, our group has used one or more one-dimensional tent functions. This means that for a system with two primary coordinates, the anchor points were located along two independent primary coordinate grids. The tertiary contribution would depend on both primary coordinates, but the contribution along one primary coordinate was independent of the other primary coordinate. As an example, if there were three anchor points along one primary coordinate and three along the other, there were six anchor points in total. In the present study, we used a two-dimensional tent function, which means that the tertiary contribution depends on a two-dimensional primary coordinate space. With two primary coordinates, this means that there are nine anchor points.

Section II briefly describes the DQ diabatization scheme and the APRP method including the modifications made here to these methods. Section II also presents the analytic forms fit to the DPEM. Section III gives the results of the DQ method and compares the

adiabatic potentials resulting from our DPEM to XMS-CASPT2, density functional, and previous theoretical and experimental studies. Section IV summarizes this paper.

Throughout this work, the ground state and the excited state in the adiabatic representation will be referred to as S_0 and S_1, respectively, the adiabatic potentials for the ground and excited states will be referred to as V_1 and V_2, respectively, the ground and excited diabatic potentials are called U_{11} and U_{22}, respectively, and the diabatic coupling is U_{12}.

For calculating zero point energies and enthalpies with the APRP surface, we used the harmonic approximation at the minimum-energy geometries of V_1 and V_2.

II. METHODS AND COMPUTATIONAL DETAILS

A. Electronic structure calculations

Electronic structure calculations were performed with the *Molpro* program package[39,40] for the ground and first excited states by XMS-CASPT2[24] with the 6-31++G(d,p)[41–45] basis set. All XMS model spaces have a dimension of 2 (S_0 and S_1 as explained above). The reference state for the perturbation calculations producing the adiabatic states used for diabatization was SA-CASSCF[46] with six active electrons in six active orbitals, denoted as (6,6), averaged over two states with equal weights.

Symmetry was turned off. To avoid intruder states, a level shift of $0.3E_h$ was applied. At this level of theory, the orbitals look satisfactory, and the calculations are fast enough to enable the optimization of the geometry of the ground and excited states and to calculate adiabatic energies at the large number of geometries required as an input for diabatization and fitting.

B. Diabatization

The calculations described in Subsection II A yield electronically adiabatic energies. As discussed in Sec. I, these are not smooth functions of nuclear coordinates; the adiabatic potentials have cuspidal ridges along conical intersection seams. Furthermore, the adiabatic states are coupled by nonadiabatic couplings (NACs), which are vectors resulting from the action of the nuclear momentum operator on the adiabatic electronic wave functions, and these become singular along the conical intersection seams. These features make the NACs and adiabatic potentials impractical to fit.

In the present study, there are two adiabatic surfaces, which are transformed into a 2 × 2 diabatic potential energy matrix (DPEM), whose elements are matrix elements of the electronic Hamiltonian in the diabatic basis, in which this Hamiltonian is not diagonal. The diagonal elements are the diabatic surfaces U_{11} and U_{22}; the off-diagonal element is the diabatic coupling U_{12}. If the diabatization is successful, it circumvents the fitting problem of the previous paragraph by producing a DPEM where matrix elements are smooth functions of the nuclear coordinates, and the electronic states are smooth enough that the operation of the nuclear momentum operators on them may be neglected. Thus, in a diabatic representation, the coupling is provided by the smooth scalar off-diagonal elements of the electronic Hamiltonian (the diabatic couplings) rather than by singular NAC vectors, and the potential energy surfaces (the diabatic potentials) are smooth enough to be fit by analytic functions. The diabatic Hamiltonian can be transformed back to the adiabatic Hamiltonian by diagonalization, and the diabatization procedure we use is adiabatic equivalent, which means that the diabatic state functions span the same space as the two lowest adiabatic state functions so that the adiabatic potentials one gets by diagonalization are the original ones.

Diabatization was done using the DQ diabatization method published previously.[33,34] This method makes use of two electronic properties, the dipole moment, and the quadrupole moment, to distinguish diabatic states. These properties are defined as

$$\boldsymbol{\mu} = \sum_{i=1}^{N_{el}+N_{nuc}} q_i \mathbf{r}_i, \tag{1}$$

$$Q^{(j)} = \sum_{i=1}^{N_{el}+N_{nuc}} q_i |\mathbf{r}_i - \mathbf{r}_j|^2, \tag{2}$$

where $\boldsymbol{\mu}$ is the dipole operator, q_i is the charge of particle i, $\mathbf{r}_i$ is the coordinate of particle i, and $Q^{(j)}$ is the traceless quadrupole at an origin, $\mathbf{r}_j$. The DQ method is carried out by maximizing

$$f_{\mathrm{DQ}} = \sum_{s=1}^{N_{\mathrm{states}}} \left(w_\mu |\langle \psi_s | \boldsymbol{\mu} | \psi_s \rangle|^2 + \sum_{j=1}^{N_Q} w_j \left| \left\langle \psi_s \middle| Q^{(j)} \middle| \psi_s \right\rangle \right|^2 \right) \tag{3}$$

where ψ_s is diabatic state s, w_μ is a user determined weight on the dipole moment, w_j is a user determined weight at the quadrupole term at origin j, and N_{states} is the total number of states (2 in the present case). Diabatic states are defined as linear combination of adiabatic states,

$$\psi_s = \sum_{I=1}^{N_s} \phi_s T_{sA}, \tag{4}$$

where ϕ_s are adiabatic states and $\mathbf{T}$ is a transformation matrix. The DQ method solves for the transformation that maximizes f_{DQ}.

In this work, quadrupole origins were placed at each hydrogen (five sites) and at the carbon atom. Previous work with the DQ method on smaller systems mainly utilized constant weights on the different quadrupole contributions. For the present system, no constant weights we tried could give good diabatic potentials for all the regions tested. To overcome this problem, we used coordinate-dependent weights. The weights for the quadrupole moments at the hydrogen atoms are defined as

$$w_{\mathrm{H}x}(r_{\mathrm{N-H}x}) = \omega_{\mathrm{QH}} e^{-a_{\mathrm{N-H}} \cdot \left(r_{\mathrm{N-H}x} - r_{\mathrm{N-H}}^{[0]} \right)}, \tag{5}$$

where $w_{\mathrm{H}x}$ is the weight in Eq. (3) for the quadrupole contribution at Hx (x can be 1, 2, 5, 6, or 7; see Fig. 1), $r_{\mathrm{N-H}x}$ is the N–Hx distance, ω_{QH} and a_{NH} are parameters, and $r_{\mathrm{NH}}^{[0]}$ is the ground-state equilibrium N–H distance. The weight on the quadrupole moments with their origin at the carbon is

$$w_{\mathrm{C}}(r_{\mathrm{C-N}}) = \omega_{\mathrm{QC}} e^{-b_{\mathrm{C-N}} \cdot \left(r_{\mathrm{C-N}} - r_{\mathrm{C-N}}^{[0]} \right)^2}, \tag{6}$$

where w_{C} is the weight in Eq. (3) for the quadrupole contribution at C, $r_{\mathrm{C-N}}$ is the C–N distance, ω_{QC} and b_{CN} are parameters, and $d_{\mathrm{CN}}^{[0]}$ is the ground-state equilibrium C–N distance. The parameters for Eqs. (5) and (6) are given in Table I. The dipole weight, w_μ, was 1 a_0^{-1} for all diabatization calculations in this study. Diabatization with these specifications led to smooth diabatic potentials in the regions tested.

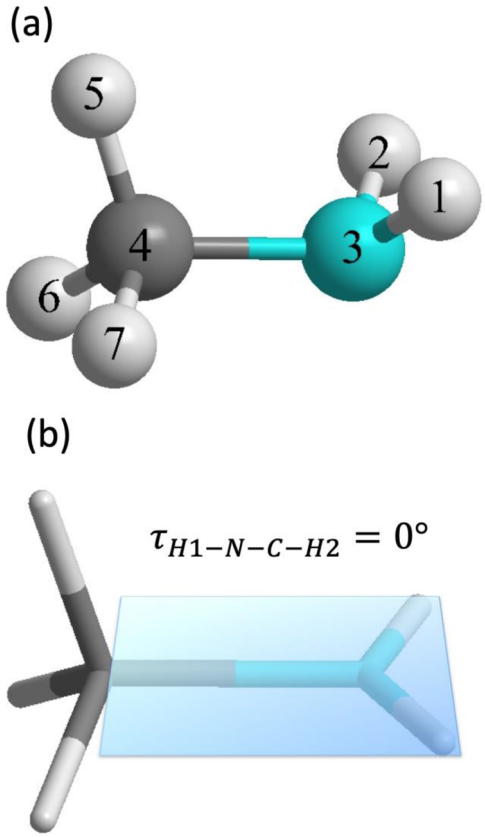

FIG. 1. Methylamine with naming conventions (a) at the optimized ground-state geometry and (b) with the H1–N–C–H2 improper torsion set to 0°.

C. Analytic potential energy matrix

The notation in Fig. 1 will be used to describe coordinates and structures. Panel b shows the structure when the four atoms of the CNH_2 moiety lie in the same plane. Motion that simultaneously takes H1 and H2 above or below this plane is referred to as the amino wag.

Methylamine has 15 internal degrees of freedom, which is too many for a fully global multi-surface fit, and so it was necessary to prioritize certain regions of geometry to be fit with faithful accuracy; this determination was based on the goal of creating a DPEM suitable for simulating the photodissociation of an N–H bond. Upon photoexcitation, methylamine can dissociate via multiple pathways forming different products; it can dissociate by breaking an N–H, C–N, or C–H bond. The N–H bond dissociation gives the highest yield in experiments with excitation into the first ultraviolet absorption band.[1,2,6–13] The dissociated hydrogens have a bimodal translational energy distribution, and the dynamics show mode dependency.[6,7,13–15] Previous work has found evidence of conical intersections along the N–H stretch when the amine has a planar geometry,[3–5] and we anticipate the motion of the NH_2 "wag," which changes the amino structure between planar and pyramidal, to be important in understanding the system behavior upon photoexcitation. We use the H1–N–C–H2 improper torsion angle as a measure of the wag coordinate. Toward our goal of creating a PEM suitable for simulating the N–H photodissociation experiments, the N–H1 bond coordinate and H1–N–C–H2 improper torsion angle are taken as primary coordinates in the APRP scheme[35] and are fitted globally with the other coordinates held fixed. All other coordinates are considered to be spectator coordinates and are treated as tertiary coordinates. The tertiary coordinates are taken as the N–H2 stretch, two C–N–H bends, the C–N stretch, multiple N–C–H bends, C–H stretches, H–C–H bends, and torsions of the methyl and carbonyl hydrogens.

This partition of the coordinates means that we are not treating the two amino hydrogens in a permutationally invariant way, but we do treat the methyl hydrogens in a permutationally invariant way.

TABLE I. Parameters for Eqs. (5) and (6).

Parameter	Values
ω_{QH} (a_0^{-2})	2.0
a_{NH} ($Å^{-1}$)	3.0
$r_{NH}^{[0]}$ (Å)	1.015 75
ω_{QC} (a_0^{-2})	10.0
b_{CN} ($Å^{-2}$)	7.0
$r_{CN}^{[0]}$ (Å)	1.459 744

D. Overview of the fit

For fitting the diabatic potential energy matrix (DPEM), we calculated diabatic energies and couplings at a large number of geometries by the methods discussed above. First calculations were performed on a two-dimensional coordinate grid with the methyl group geometry fixed at the optimized ground-state equilibrium geometry. The grid has the N–H1 stretch varied from 0.6 Å to 12 Å and the H1–N–C–H2 improper torsion varied from 170° to 0°. The stretch coordinate was varied by 0.1 Å increments at small bond distances and by larger increments at larger bond distances. The improper torsion was varied by 10° increments. The improper torsion coordinate is convenient because it does not depend on N–H stretches and C–N–H bends of the amino group, which are accounted for in the other primary coordinate and in the tertiary coordinates.

In contrast to previous APRP studies,[35–38] which used local quadratic information (Hessians) to fit the tertiary coordinates, in this study, energies were directly calculated for finite displacements along tertiary coordinates and fit locally to system-specific functional forms. This was done to give a greater flexibility to the dependence of the DPEM on tertiary coordinates. The full list of tertiary coordinates studied in this way is the following: the H1–N–C bend, the H2–N–C bend, the H2–N stretch, the C–N stretch, the H7–C stretch, and the H6–C–N bend. Tertiary stretches were varied by 0.1 Å at small bond distances with larger spacing as the bond distance increases. The bend angles were varied by increments of 2°–10°. These calculations were performed with the primary coordinates held, in turn, at each of the anchor point structures, as will be detailed in Sec. II E on the tertiary fit.

Although the form of the present APRP differs from previous APRPs in some ways, we maintained the method's reliance on physically motivated functional forms along all coordinates. This feature of the APRP makes it possible to avoid introducing unphysical features into the surfaces where the energy would drop drastically below zero (often referred to as holes when produced by other methods of surface fitting). This is an advantage of APRP over methods that rely on extrapolation and/or interpolation, for example, machine-learning algorithms or least-squares fits to a dataset.

E. Primary fit

Parameters for all primary fit equations can be found in the supplementary material and in the Fortran subroutine, available both as the supplementary material and in an online potential library.[47] The U_{11} potential was fit to

$$\begin{aligned} U_{11}(r_{\text{N-H1}}, \tau_{\text{H1-N-C-H2}}) &= \kappa_x^{[11]}\left(1 - e^{-a_x^{[11]}(r-r_0)}\right)^2 + \kappa_y^{[11]} e^{-b_y^{[11]}\left(r-l_y^{[11]}\right)^2} \\ &+ \kappa_z^{[11]}\left(\cos(\tau) - \cos(\tau_0)\right)^2 \cdot e^{-b_z^{[11]}\left(r-l_z^{[11]}\right)^2} \\ &+ \sum_{i=1}^{4} \kappa_i^{[11]}\left(e^{-\beta_i^{[11]}\left(\cos(\tau)-t_i^{[11]}\right)^2}\right) \cdot \left(e^{-b_i^{[11]}\left(r-l_i^{[11]}\right)^2}\right) \end{aligned} \tag{7}$$

with parameters given in Table S1 of the supplementary material. In Eq. (7), U_{11} depends on the N–H1 distance ($r_{\text{N-H1}}$) and the H1–N–C–H2 improper torsion coordinate ($\tau_{\text{H1-N-C-H2}}$). For these coordinates, subscripts are removed from the right hand side for brevity. In the first term, r_0 is the N–H1 equilibrium bond distance. The first and second terms are a Morse potential and Gaussian that fit the NH bond stretch with all other coordinates fixed at the ground-state equilibrium geometry. In the third term, the parameter τ_0 is the improper torsion angle of the ground-state equilibrium structure. At small N–H1 bond distances, this term grows along the amino wag displacement that pushes the two hydrogen atoms away from the ground-state equilibrium structure. As the N–H1 bond distance increases, this term goes to zero due to the Gaussian to account for the absence of interactions between the two hydrogens when H1 dissociates. The fourth term is a summation of four Gaussians. This term also goes to zero as the N–H1 bond distance increases. The parameters were determined using the solver function in *Excel*. (Solver was used for all the following fits as well.) Equation (7) uses the cosine of the improper torsion angle rather than the angle itself, which enforces the property that U_{11} does not depend on the sign of the improper torsion. (All the following primary fits are also independent of the sign of the improper torsion.)

The U_{22} potential was fit to

$$\begin{aligned} U_{22}(r_{\text{N-H1}}, \tau_{\text{H1-N-C-H2}}) &= c_x^{[22]} + \kappa_x^{[22]} e^{-a_x^{[22]}\left(r-l_x^{[22]}\right)} \\ &+ \left(\kappa_y^{[22]}\left(r - d_x^{[22]}\right)^2\right) e^{-b_y^{[22]}\left(r-l_y^{[22]}\right)^2} \\ &+ \kappa_z^{[22]}\left(\cos(\tau) - 1\right)^2 \cdot e^{-b_z^{[22]}\left(r-l_z^{[22]}\right)^2} \\ &+ \sum_{i=1}^{5} \kappa_i^{[22]}\left(e^{-\beta_i^{[22]}\left(\cos(\tau)-t_i^{[22]}\right)^2}\right) \cdot \left(e^{-b_i^{[22]}\left(r-l_i^{[22]}\right)^2}\right). \end{aligned} \tag{8}$$

In Eq. (8), the first three terms are a fit along the N–H1 bond stretch with the amino hydrogens flat in a plane [Fig. 1(b)] and all other coordinates at the ground-state equilibrium structure. In the fourth term, the value, 1, comes from taking the cosine of the improper torsion angle when the amino structure is flat [$\cos(0°) = 1$]. This term grows as the amino hydrogens approach one another. Similar to the U_{11} equation, the contribution from this term goes away as the N–H1 bond dissociation coordinate increases. The final term is a summation of five Gaussians, which also goes to zero as the N–H1 bond distance increases. The parameters can be found in Table S2.

The diabatic coupling, U_{12}, is described along the two-dimensional primary coordinate grid by

$$\begin{aligned} U_{12}(r_{\text{N-H1}}, \tau_{\text{H1-N-C-H2}}) &= \sum_{j=1}^{4}\left(e^{-b_j^{[12]}\left(r-l_j^{[12]}\right)^2}\right) \cdot \left[\kappa_j^{[12]} + \zeta_j^{[12]}\sqrt{1.1 - \cos(\tau)^2}\right. \\ &\left. + \sum_{i=1}^{2} \xi_{ij}^{[12]}\left(e^{-\beta_{ij}^{[12]}\left(\cos(\tau)-t_{ij}^{[12]}\right)^2}\right)\right]. \end{aligned} \tag{9}$$

Similar to the equations for the diabatic potentials, this equation uses Gaussians along the stretch and improper torsion coordinates. The improper torsion angle also makes use of a semicircle-like equation with radius $(1.1)^{1/2}$. By setting the radius to $(1.1)^{1/2}$ instead of 1, the derivative is defined at 0° and 180°. U_{12} goes to zero as the N–H1 stretch distance increases to dissociation, which means that the diabatic potentials approach the adiabatic potentials in that limit. The parameters are given in Table S3.

F. Tertiary fit

The tertiary coordinates are the N–H2 and C–N stretches, three C–H stretches, the C–N–H1 and C–N–H2 bends, three N–C–H bends, three H–C–H bends, and the H2–N–C–H1 torsion. The tertiary contribution also depends (parametrically) on the primary coordinates. In the original APRP paper,[35] harmonic terms parameterized with Hessians were used for tertiary contributions, which made the dissociation of the tertiary bonds impossible. In this work, the tertiary contributions were derived by fitting electronic structure data points. The tertiary fit parameters were determined at specified locations along the two primary coordinates; these are the anchor points. Two-dimensional tent functions that depend on the primary coordinates were used to interpolate the tertiary contribution between the anchor points.

The equations for the tertiary coordinates are given in this section. The parameters for these equations at all the anchor points are given in the supplementary material in Tables S4–S26. In the equations, the superscripts in square brackets, $[n, m]$, are an indexing system for the anchor points. The functional forms of the tertiary contributions are the same for U_{11} and U_{22}, but the parameters are different. The diabatic coupling, U_{12}, takes a different form from U_{11} and U_{22} for all tertiary coordinates.

The functional form for the N–C–Hx bends is

$${}_{JJ}U_{\text{N-C-H}x}^{[n,m]} = F_{\text{N-C-H}}^{[n,m]} \cdot \left(\theta_{\text{N-C-H}x} - \theta_{\text{N-C-H}}^{0\,[n,m]}\right)^2, \tag{10}$$

where x can be 5, 6, or 7. The subscript in front of the U indicates the surface (JJ = 11 or 22). This notation is removed from the right

hand side for brevity. In this equation, $F_{\text{N-C-H}}^{[n,m]}$ is an anchor point dependent parameter; ${\theta^0_{\text{N-C-H}}}^{[n,m]}$ is the angle of minimum energy as a function of bending at anchor point $[n, m]$ (this is a simplification for the three bends because they have slightly different values along the anchor points). The parameters at every anchor point are given in Tables S4 and S5 for ground and excited states, respectively. The tertiary contribution to the U_{12} element was set to zero for displacement along this coordinate because the adiabatic potentials are essentially equal to the diabatic potentials along the N–C–H bends.

The form for the C–Hx stretches is given by

$$ {}_{JJ}U_{\text{C-H}x}^{[n,m]} = F_{\text{C-H}}^{[n,m]} \cdot \left(1 - e^{-{a_{\text{C-H}}}^{[n,m]}\left(r_{\text{C-H}x} - {r^0_{\text{C-H}}}^{[n,m]}\right)}\right)^2, \tag{11} $$

where x can be 5, 6, or 7. This equation has parameters, $F_{\text{C-H}}^{[n,m]}$ and ${a_{\text{C-H}}}^{[n,m]}$. The parameter ${r^0_{\text{C-H}}}^{[n,m]}$ is the minimum energy stretch distance at anchor point $[n, m]$ (this is a slight simplification as the three stretches actually have slightly different values). The parameter values are given in Tables S6 and S7 for the ground and excited states, respectively. The equation is a Morse potential, which allows the bond to dissociate. The tertiary contribution to U_{12} for displacement along this coordinate was set to zero because the adiabatic potentials are essentially equal to the diabatic potentials along the C–H stretch.

The functional form of contributions along the N–H2 stretch for U_{11} and U_{22} is given by

$$ {}_{JJ}U_{\text{N-H2}}^{[n,m]} = F_{\text{N-H2}}^{[n,m]} \cdot \left(1 - e^{-{a_{\text{N-H2}}}^{[n,m]}\left(r_{\text{N-H2}} - {r^0_{\text{N-H2}}}^{[n,m]}\right)}\right)^2 + G_{\text{N-H2}}^{[n,m]} \cdot \left(r_{\text{N-H2}} - {r^0_{\text{N-H2}}}^{[n,m]}\right)^4. \tag{12} $$

The first term is a Morse potential with parameters $F_{\text{N-H2}}^{[n,m]}$, ${a_{\text{N-H2}}}^{[n,m]}$, and ${r^0_{\text{N-H2}}}^{[n,m]}$, which is the minimum-energy stretch at the anchor point $[n, m]$. The second term is a simple quartic function of $r_{\text{N-H2}}$ centered at ${r^0_{\text{N-H2}}}^{[n,m]}$, with leading coefficient, $G_{\text{N-H2}}^{[n,m]}$. This second term prevents the N–H2 bond from dissociating, which is a major restriction made for our DPEM to be discussed in more detail in Sec. III, but we mention here that this is one reason why the DPEM is semiglobal rather than being globally accurate for all possible geometries. The parameter values for the ground and excited states are given in Tables S8 and S9, respectively.

The tertiary contribution to U_{12} along the N–H2 stretch is

$$ {}_{IJ}U_{\text{N-H2}}^{[n,m]} = H_{\text{N-H2}}^{[n,m]} \cdot e^{-{\omega_{\text{N-H2}}}^{[n,m]}\left(r_{\text{N-H2}} - {\lambda_{\text{N-H2}}}^{[n,m]}\right)^2}. \tag{13} $$

This equation is a Gaussian with parameters $H_{\text{N-H2}}^{[n,m]}$, ${\omega_{\text{N-H2}}}^{[n,m]}$, and ${\lambda_{\text{N-H2}}}^{[n,m]}$ whose values are in Table S10.

The tertiary contributions to the diabatic potentials and diabatic coupling for the C–N stretch have the same functional form as N–H2 [Eqs. (12) and (13)]. The values for these parameters at all the anchor points are given in Tables S11–S13 for U_{11}, U_{22}, and U_{12}, respectively. These parameters have the same naming convention as for Eqs. (12) and (13), but the N–H2 subscript is replaced by C–N.

The functional form of the C–N–Hx tertiary contributions for U_{11} and U_{22} are given in Eq. (14), where x is 1 or 2; the parameters for these two bends are very similar for anchor points at small N–H1 distances, but the C–N–H1 contribution goes to zero at large N–H1 distances. The equation has parameters $F_{\text{C-N-H}x}^{[n,m]}$ and ${\theta^0_{\text{C-N-H}x}}^{[n,m]}$, which is the minimum energy bend at the anchor point $[n, m]$ for the bend, C–N–Hx. The tertiary contribution to U_{12} for both bends has a Gaussian form as shown in Eq. (15), with parameters $H_{\text{C-N-HX}}^{[n,m]}$, ${\omega_{\text{C-N-H}x}}^{[n,m]}$, and ${\lambda_{\text{C-N-H}x}}^{[n,m]}$. The parameters for these equations are given in Tables S14–S19 in the order: U_{11}, U_{22}, U_{12} for $x = 1$, then U_{11}, U_{22}, U_{12} for $x = 2$,

$$ {}_{JJ}U_{\text{C-N-H}x}^{[n,m]} = F_{\text{C-N-H}x}^{[n,m]} \cdot \left(\cos(\theta_{\text{C-N-H}x}) - \cos\left({\theta^0_{\text{C-N-H}x}}^{[n,m]}\right)\right)^2, \tag{14} $$

$$ {}_{IJ}U_{\text{C-N-H}x}^{[n,m]} = H_{\text{C-N-H}x}^{[n,m]} \cdot e^{-{\omega_{\text{C-N-H}x}}^{[n,m]}\left(\cos(\theta_{\text{C-N-H}x}) - {\lambda_{\text{C-N-H}x}}^{[n,m]}\right)^2}. \tag{15} $$

In addition to the tertiary equations given above, with parameters fitted to *ab initio* electronic structure data, we also included two tertiary functions based on qualitative considerations. To account for amino group rotation relative to the methyl group, we included

$$ {}_{JJ}U_{\text{H2-N-C-H5}}^{[n,m]} = H_{\text{H2-N-C-H5}}^{[n,m]} \cdot (1 - \cos 3(\tau_{\text{H2-N-C-H5}} - \tau_T)) \times e^{\frac{(r_{\text{H2-H5}} - d_{\text{H2-H5}})^2}{-\omega_{\text{H2-H5}}}}. \tag{16} $$

In this equation, the amino and methyl hydrogens interact through a torsion term. The term becomes smaller at larger H2–H5 bond lengths due to the Gaussian term. The contribution from this equation was very small, but we saw a clear improvement in frequency calculations with its addition. The N–H1 torsion is not included in this tertiary contribution because attempting to include it caused small but unphysical adjustments to the minimum-energy structures. The parameters ($H_{\text{H2-N-C-H5}}^{[n,m]}$, $d_{\text{H2-H5}}$, τ_T, and $\omega_{\text{H2-H5}}$) are given in Tables S20 and S21 for U_{11} and U_{22}, respectively. Only the parameter, $H_{\text{H2-N-C-H5}}^{[n,m]}$, is dependent on the anchor point. No contribution to U_{12} was included for this tertiary coordinate.

The contribution from the three H–C–H bends on the methyl was included by

$$ {}_{JJ}U_{\text{H-C-H}}^{[n,m]} = \sum_{X<Y} H_{\text{H-C-H}}^{[n,m]} \cdot (\theta_{\text{H}x\text{-C-H}y} - \lambda_{\text{H-C-H}})^2 \cdot e^{\frac{(y - d_{\text{H-H}})^2}{-\omega_{\text{H-H}}}}, \tag{17} $$

which is a pairwise summation of the three interactions. In this equation, x and y can be 5, 6, or 7, but x cannot equal y. The contribution from these terms is small, but again we saw an improvement in our frequency calculations when it was included. The contributions from a HCH interaction will go to zero if one of those C–H bonds break due to the Gaussian term. The parameters ($H_{\text{H-C-H}}^{[n,m]}$, $\lambda_{\text{H-C-H}}$, $d_{\text{H-H}}$, and $\omega_{\text{H-H}}$) for U_{11} and U_{22} are given in Tables S22 and S23, respectively. Only the parameter, $H_{\text{H-C-H}}^{[n,m]}$, is dependent on the anchor point. No contribution was included for U_{12} for this tertiary coordinate.

The tertiary potential at an anchor point is the sum of all the tertiary contributions at that anchor point and a constant, ${}_{IJ}const^{[n,m]}$,

$$ {}_{IJ}U^{[n,m]}(\boldsymbol{R}) = \sum_{stretches} {}_{IJ}U^{[n,m]}_{stretch} + \sum_{bends} {}_{IJ}U^{[n,m]}_{bend} + {}_{IJ}const^{[n,m]}, \quad (18) $$

where ${}_{IJ}U^{[n,m]}(\boldsymbol{R})$ is the tertiary energy contribution at anchor point $[n, m]$ for the diabatic state, IJ, where I can equal J. The **R** stands for all the tertiary coordinates. The constants are given in Table S24. They were calculated by solving for the tertiary contribution at each anchor point with the tertiary coordinates at the ground state minimum structure and multiplying this energy contribution by −1. The constants adjust the zero of energy so when the tertiary coordinates are at the ground state optimized structure and the primary coordinates are at anchor points, the total energy will equal the energy of the primary coordinate fit (i.e., the tertiary contribution will be zero). At other structures, the tertiary contribution could result in a total energy that is lower or higher than the primacy contribution depending on the tertiary coordinates' minimum structures at every anchor point.

Previous work with APRP has involved one-dimensional tent functions.[35–38] For this system, we have generalized that approach to two dimensions. As can be seen in the equations above, the tertiary contributions and tent functions have a two index naming convention; the first term in brackets, n, corresponds to the index along $r_{\mathrm{N-H1}}$ and the second term, and m is the index along $\cos(\tau_{\mathrm{H1-N-C-H2}})$. The interpolation between the tertiary contributions at the different anchor points (${}_{IJ}U_{Tertiary}$) is calculated by

$$ {}_{IJ}U_{\mathrm{Tertiary}} = \sum_{n=1}^{4}\sum_{m=1}^{3} {}_{IJ}U^{[n,m]}(\boldsymbol{R}) \cdot T^{[n,m]}(r_{\mathrm{N-H1}}, \tau_{\mathrm{H1-N-C-H2}}). \quad (19) $$

In this equation, $T^{[n,m]}(r_{\mathrm{N-H1}},\tau_{\mathrm{H1-N-C-H2}})$ is the tent function. These anchor points are located at four N–H1 bond distances at approximately 0.7 Å, 1.0 Å, 2.2 Å, and 3.5 Å and at three H1–N–C–H2 improper torsions at approximately 0° (which corresponds to planar CNH_2), 61° (the optimized improper torsion), and 100° (a higher-energy structure with H1 and H2 closer to each other). This yields 12 anchor points; a schematic of the anchor points is shown in Fig. 2. The leftmost anchor points are located at cos(100°) and the right most points are at cos(0°).

All three anchor points with N–H1 at 3.5 Å along the torsion coordinate are given equivalent parameters, that is, ${}_{IJ}U^{[4,m]}(\boldsymbol{R})$ was the same for all m. At this distance along the N–H1 bond length, the improper torsion has a negligible effect because the two hydrogens stop interacting. In Fig. 2, these anchor points at N–H1 = 3.5 Å are shown along a red, dashed line.

An example is shown in Eqs. (20)–(23) of the four nonzero tent functions, T, at the [1, 1] anchor point, which depends on the values of the two primary coordinates (shortened to r and τ). The tent function for a general anchor point, (p, q), is given in Eqs. (24)–(27). When the coordinates do not fall between tent function's anchor points, that tent function is zero. For example, when the primary coordinates are smaller than $r^{[1]}$ and $\cos(\tau)^{[1]}$ [Eq. (20)], all the tent terms except for $T^{[1,1]}$ are equal to zero ($T^{[1,2]} = T^{[1,3]} = T^{[2,2]} = \cdots = T^{[3,3]} = 0$),

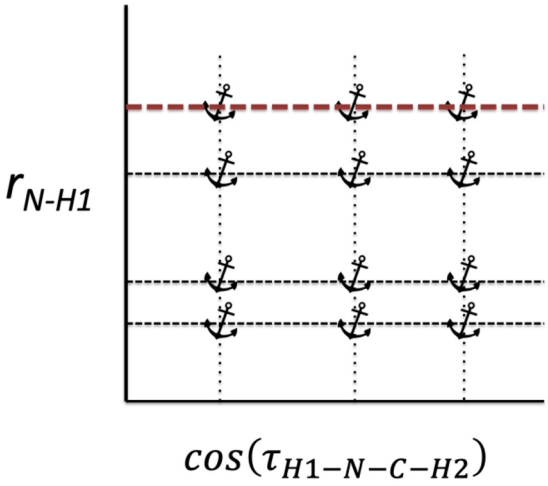

FIG. 2. Schematic of anchor point locations along the primary coordinates.

$$ T^{[1,1]} = 1 \quad \begin{cases} r < r^{[1]} \\ \cos(\tau) < \cos(\tau)^{[1]}, \end{cases} \quad (20) $$

$$ T^{[1,1]} = \frac{\left(r - r^{[2]}\right)^4 \left(\cos(\tau) - \cos(\tau)^{[1]}\right)^4}{\sum_{\chi=1}^{2} \left(r - r^{[\chi]}\right)^4 \left(\cos(\tau) - \cos(\tau)^{[1]}\right)^4}, \quad \begin{cases} r^{[1]} \le r < r^{[2]} \\ \cos(\tau) < \cos(\tau)^{[1]}, \end{cases} \quad (21) $$

$$ T^{[1,1]} = \frac{\left(r - r^{[1]}\right)^4 \left(\cos(\tau) - \cos(\tau)^{[2]}\right)^4}{\sum_{\eta=1}^{2} \left(r - r^{[1]}\right)^4 \left(\cos(\tau) - \cos(\tau)^{[\eta]}\right)^4}, \quad \begin{cases} r < r^{[1]} \\ \cos(\tau)^{[1]} \le \cos(\tau) < \cos(\tau)^{[2]}, \end{cases} \quad (22) $$

$$ T^{[1,1]} = \frac{\left(r - r^{[2]}\right)^4 \left(\cos(\tau) - \cos(\tau)^{[2]}\right)^4}{\sum_{\chi=1}^{2}\sum_{\eta=1}^{2} \left(r - r^{[\chi]}\right)^4 \left(\cos(\tau) - \cos(\tau)^{[\eta]}\right)^4}, \quad \begin{cases} r^{[1]} \le r < r \\ \cos(\tau)^{[1]} \le \cos(\tau) < \cos(\tau)^{[2]}, \end{cases} \quad (23) $$

$$ T^{[p,q]} = \frac{\left(r - r^{[p-1]}\right)^4 \left(\cos(\tau) - \cos(\tau)^{[q-1]}\right)^4}{\sum_{\chi=p-1}^{p}\sum_{\eta=q-1}^{q} \left(r - r^{[\chi]}\right)^4 \left(\cos(\tau) - \cos(\tau)^{[\eta]}\right)^4}, \quad \begin{cases} r^{[p-1]} \le r < r^{[p]} \\ \cos(\tau)^{[q-1]} \le \cos(\tau) < \cos(\tau)^{[q]}, \end{cases} \quad (24) $$

$$T^{[p,q]} = \frac{\left(r - r^{[p+1]}\right)^4 \left(\cos(\tau) - \cos(\tau)^{[q-1]}\right)^4}{\sum_{\chi=p}^{p+1} \sum_{\eta=q-1}^{q} \left(r - r^{[\chi]}\right)^4 \left(\cos(\tau) - \cos(\tau)^{[\eta]}\right)^4},$$
$$\begin{cases} r^{[p]} \le r < r^{[p+1]} \\ \cos(\tau)^{[q-1]} \le \cos(\tau) < \cos(\tau)^{[q]}, \end{cases} \quad (25)$$

$$T^{[p,q]} = \frac{\left(r - r^{[p-1]}\right)^4 \left(\cos(\tau) - \cos(\tau)^{[q+1]}\right)^4}{\sum_{\chi=p-1}^{p} \sum_{\eta=q}^{q+1} \left(r - r^{[\chi]}\right)^4 \left(\cos(\tau) - \cos(\tau)^{[\eta]}\right)^4},$$
$$\begin{cases} r^{[p-1]} \le r < r^{[p]} \\ \cos(\tau)^{[q]} \le \cos(\tau) < \cos(\tau)^{[q+1]}, \end{cases} \quad (26)$$

$$T^{[p,q]} = \frac{\left(r - r^{[p+1]}\right)^4 \left(\cos(\tau) - \cos(\tau)^{[q+1]}\right)^4}{\sum_{\chi=p}^{p+1} \sum_{\eta=q}^{q+1} \left(r - r^{[\chi]}\right)^4 \left(\cos(\tau) - \cos(\tau)^{[\eta]}\right)^4},$$
$$\begin{cases} r^{[p]} \le r < r^{[p+1]} \\ \cos(\tau)^{[q]} \le \cos(\tau) < \cos(\tau)^{[q+1]}. \end{cases} \quad (27)$$

III. RESULTS AND DISCUSSION

Subsection III A considers only the direct results of the DQ diabatization (without fitting), and Subsections III B–III F consider the results obtained from the fits. In Subsections III B and III D, we will compare some of our results to experiment and to the following previous calculations:

- XMS13 direct (i.e., not fitted) MS-CASPT2 calculations with a SA-CASSCF(8,8) reference function by Xiao *et al.*[5]
- TLM14 CCSD and EOM-CCSD calculations by Thomas *et al.*[17]
- LGH18 CC3 adiabatic calculations by Loos *et al.*[22]
- WXGY19 results calculated from a DPEM fit to MR-CISD calculations with a SA-RASSCF reference function by Wang *et al.*[16]

In Subsections III B–III E, we will present some comparisons of adiabatic potentials computed from the DPEM fit to directly calculate adiabatic results, and Subsection III E shows some comparison of the APRP DPEM to the values that were fit.

A. Diabatization

Before showing results from the fitted potentials, this section first gives the direct results without fitting; adiabatic energies and diabatic energies are shown in Fig. 3 for slices along the (a) N–H1, (b) C–H7, and (c) C–N stretch. All other internal coordinates have their ground-state equilibrium values. For the slices shown in this figure, the adiabatic energies are widely separated. For the N–H and C–N stretches, the diabatic potentials cross, while along the C–H stretch, there is not a crossing, and the diabatic potentials are approximately equal to the adiabatic potentials. This is consistent with previous findings[3,4] that the N–H and C–N dissociations involve a change in character of the S_0 and S_1 states, while C–H dissociation does not. This change in character comes from the evolution of the p orbitals along the N–H and C–N dissociation pathways; the ground state at the equilibrium structure evolves diabatically to the excited state at dissociation, and the excited state at the equilibrium structure evolves diabatically to the ground state at dissociation.

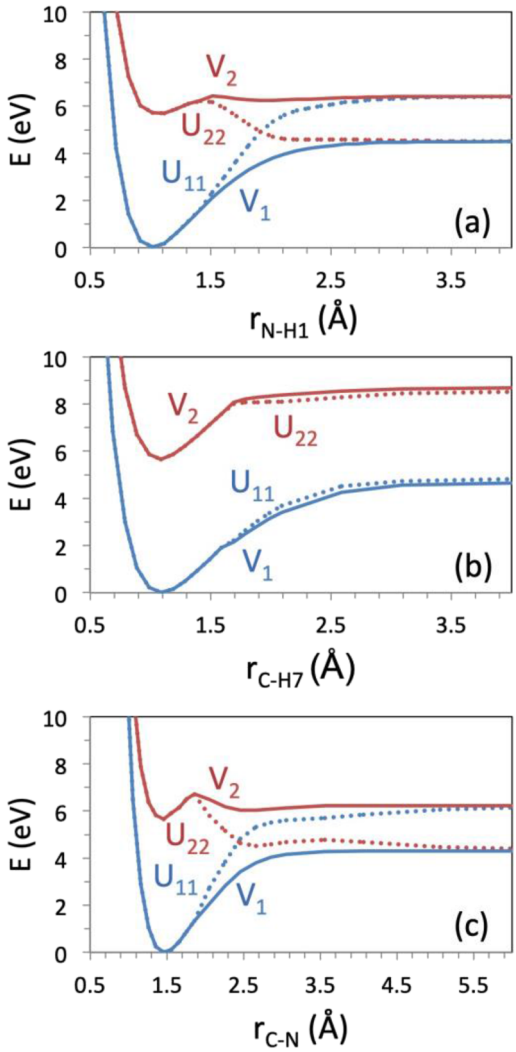

FIG. 3. Adiabatic potentials and DQ diabatic potentials along three bond dissociation coordinates: (a) N–H1, (b) C–H7, and (c) C–N.

As mentioned already, in previous work where we studied small test systems using the DQ method, we mainly used constant weights on the quadrupole terms,[33,34] but for the present system, we were not able to find constant weights that worked along different slices, and therefore, we switched to coordinate-dependent weights, as described in Sec. II. Figure 3 shows that the results for the DQ diabatization method with coordinate-dependent weights work well. The present application to methylamine therefore supports previous findings[33,34] that the DQ diabatization method can produce smooth diabatic potentials, and it also demonstrates the usefulness

of coordinate-dependent weights on the quadrupole contribution for a polyatomic system.

B. Excitation energies and dissociation energy

The vertical excitation energy is the difference of the ground and first-excited state energies at the ground-state equilibrium geometry. Table II compares the vertical excitation energies of our APRP DPEM with adiabatic data from XMS-CASPT2(6,6) used to create the fit and with previous work. These results agree well.

Our APRP fit shows good agreement with our XMS-CASPT2(6,6) calculations indicating a good fit in this region. Our vertical excitation energies are slightly higher than those calculated by Xiao *et al.* (XMS13).[5]

The classical adiabatic excitation energy is the energy difference of the excited-state and ground-state minimum-energy structures, and the 0–0 excitation energy is the quantal adiabatic excitation energy, which is the energy difference between the zero-point levels of S_1 and S_0. In Table III, we compare the classical adiabatic and 0–0 excitation energies from the APRP surface, electronic structure calculations in the literature, and experiment.

For the classical adiabatic energy, the APRP results agree well with the XMS13 calculations but are smaller than the WXGY19 result. For the 0–0 excitation, the experimental value has been debated,[11] which is why multiple values are given in Table III. The APRP surface is in better agreement with the lower 0–0 excitation energy, but the reliability of the calculations is not high enough to cast doubt on the most recent experimental determination,[10,11] which is very convincing.

In Table IV, we compare our N–H bond dissociation enthalpy with the experiment at 298 K. Our APRP results are considerably lower than the experimental value obtained from the Active Thermochemical Tables.[48–53] Comparing our APRP fit to the XMS-CASPT2(6,6) data that were used in the fitting procedure, we see good agreement in that the equilibrium bond energies differ by only 0.03 eV. This suggests that the discrepancy with the experiment comes mainly from the electronic structure calculations and not from the fits.

Table V compares our N–H bond dissociation enthalpy with the available theoretical results in the literature at 0 K. All the theoretical calculations give too low of a bond energy. This difference from the experiment should be taken into consideration for dynamics studies with our fitted surface or that of Ref. 16.

TABLE II. Vertical excitation energies on the adiabatic potentials.

Method	Type	S_0–S_1 (eV)	Reference
APRP	From fit	5.70	This work
XMS-CASPT2(6,6)	Direct	5.65	This work
XMS13	Direct	5.57	5

TABLE III. Adiabatic and 0–0 excitation energies for the ground to first excited state of methylamine.

Method		Classical adiabatic (eV)	0–0 (eV)	References
APRP	From fit	5.08	4.89	This work
XMS13	Direct	5.03	...	5
TLM14	Direct	5.15	5.00	17
LGJ18	Direct	5.43	5.30	22
WXGY19	From fit	5.41	5.26	16
Expt. 1995			4.93	18
Expt. 2002			5.18	21
Expt. 2002–2003	...	...	5.17	10 and 11

TABLE IV. Bond dissociation enthalpy of the ground state of methylamine at 298 K including the change in zero point energy.

Method	ΔH_{298} (eV)	Reference
APRP	4.12	This work
Expt.	4.31	53

TABLE V. Bond dissociation enthalpy of the ground state of methylamine including zero point energy.

Method	ΔH_0 (eV)	Reference
APRP	4.06	This work
XMS13	4.21[a]	5
TLM14	4.00	17
WXGY19	4.17	16
Expt.	4.25	51

[a]Computed by estimating the zero-point energy contribution as −0.40 eV.

C. Equilibrium geometry and frequencies

The equilibrium geometric parameters of the S_0 state calculated with our APRP surface and with density functional theory (DFT) are shown in Table VI. The DFT calculations were performed with the M06-2X functional[54] and the 6-31++G** basis set.[41–45] Comparing the two methods shows that all geometric parameters are in good agreement. For the DFT optimized parameters, the C–H5 bond length and N–C–H5 bend angle are slightly larger than the other C–H lengths and N–C–H angles. The three C–H bond lengths and three N–C–H bond angles from APRP are equivalent because of the functional form of the APRP DPEM. As stated in Sec. II, this was a simplification we employed. We do not anticipate that this approximation will have a significant effect on future studies involving the surfaces.

The optimized structure of the methylamine excited state has, for a long time, been assigned as having a pyramidalization change from the optimized ground state.[3] This means that the amino group moves toward a more planar structure. We calculated the optimized excited state using our APRP surface and time-dependent density functional theory (TDDFT). The geometric parameters are shown in Table VII. The TDDFT calculations were performed with the τHCTHhyb functional[55] and the 6-31++G** basis set.[41–45] Before

TABLE VI. Geometric parameters of the S_0 equilibrium geometry of methylamine calculated with the APRP surfaces and DFT using M06-2X/6-31++G**.

	APRP	M06-2X
Bond lengths (Å)		
N–H1	1.02	1.01
N–H2	1.02	1.01
C–N	1.46	1.46
C–H5	1.09	1.10
C–H6	1.09	1.09
C–H7	1.09	1.09
Bond angles (deg)		
C–N–H1	111	111
C–N–H2	111	111
N–C–H5	110	115
N–C–H6	110	109
N–C–H7	110	109
Improper torsion (deg)		
H1–N–C–H2	63	61

comparing the parameters, we note an interesting, but energetically irrelevant difference in structure between the two calculations. The APRP excited structure has a "ciscoid" geometry, as defined by Xiao *et al.*,[5] where H5 is approximately in a plane with C, N, H1, and H2. This geometry was also found when optimizing the excited state using XMS-CASPT2(6,6). The TDDFT results are more similar to what Morokuma describes as a "planar" geometry, where no methyl hydrogens are in the amino plane. Xiao *et al.* found that the ciscoid structure was ~0.002 eV higher in energy than the planar geometry.[5] Because this energy difference between the structures is very small, we believe that this discrepancy is not problematic.

TABLE VII. Geometric parameters of the S_1 equilibrium geometry of methylamine calculated with the APRP surfaces and TD-DFT using τ-HCTHhyb/6-31++G**.

	APRP	τHCTHhyb
Bond lengths (Å)		
N–H1	1.06	1.03
N–H2	1.06	1.03
C–N	1.43	1.42
C–H5	1.09	1.11
C–H6	1.09	1.10
C–H7	1.09	1.10
Bond angles (deg)		
C–N–H1	120	121
C–N–H2	122	121
N–C–H5	108	106
N–C–H6	108	110
N–C–H7	108	110
Improper torsion (deg)		
H1–N–C–H2	1	10

Comparing the geometric parameters in this table, the APRP results and TDDFT are mostly very similar, except for the H1–N–C–H2 improper torsion; for TDDFT, this parameter is 10°, and for APRP, it is 1°. These measurements translate to the amino wag coordinate being slightly out of the plane for TDDFT vs the CNH_2 essentially in a plane for the APRP. For XMS-CASPT2(6,6) (used for the fit), the optimized excited state had an improper torsion value of ~4°, which is closer to our APRP value and likely contributed to the difference in this parameter compared to TDDFT calculations. Xiao *et al.* found the S_1 optimized state to have an improper torsion of 6°,[5] which falls between our results from the two electronic structure optimizations.

A small difference is noted for the C–H bond lengths and N–C–H angles; similar to the ground state, these parameters differ slightly for TDDFT, while the APRP surface treats these bond lengths and angles as being equivalent.

Figure 4 compares the vibrational frequencies of the APRP adiabatic potentials and DFT methods for S_0 [Fig. 5(a)] and S_1 [Fig. 5(b)]. The data are in good qualitative agreement. For the S_0 frequency data, the mean unsigned percentage difference between the

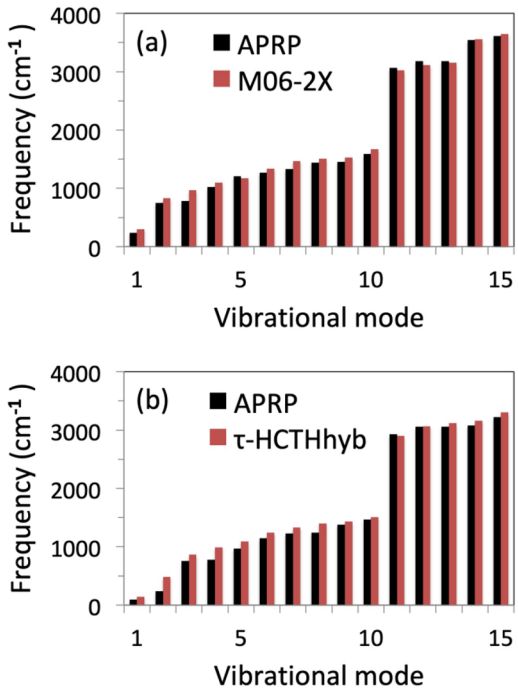

FIG. 4. Frequencies of the S_0 and S_1 equilibrium geometry of methylamine computed with APRP and with DFT using M06-2X for the ground state and TD-DFT using τ-HCTHhyb for the excited state. DFT and TDDFT calculations were done with the 6-31++G** basis set.

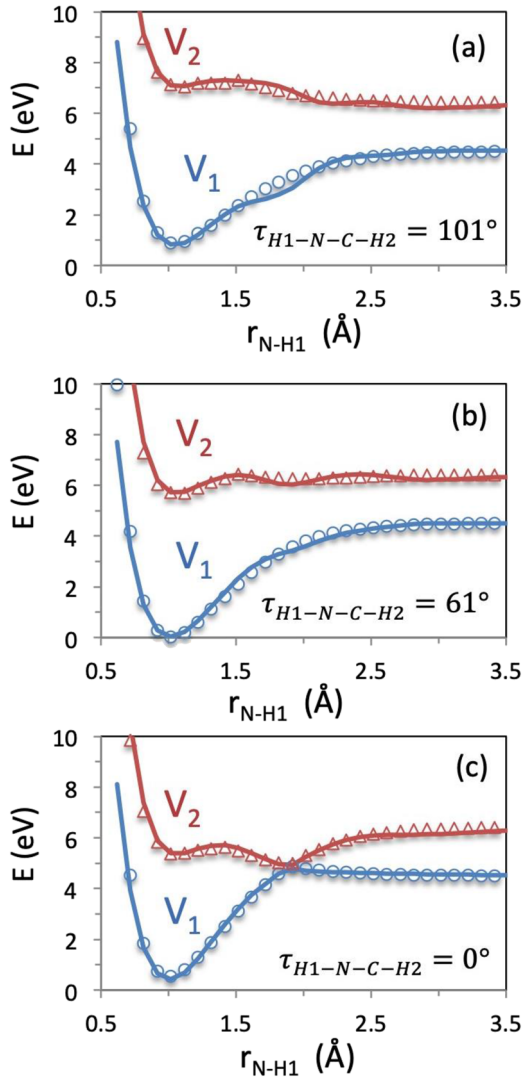

FIG. 5. Adiabatic potentials along primary coordinates, the three slices are along the N–H1 dissociation coordinate with the H1–N–C–H2 improper torsion at (a) 101°, (b) 61°, and (c) 0°. APRP results are the lines, and XMS-CASPT(6,6) results are the circles and triangles.

two methods is 8%. Removing the frequencies lower than 1000 cm^{-1}, the unsigned percentage difference improves to 5%. For the S_1 data, the mean unsigned percentage difference is 16%, and removal of frequencies lower than 1000 cm^{-1} gives an improved mean unsigned percentage difference of 6%. These results are encouraging for our modified APRP approach. Previous APRP studies relied on Hessian data from DFT calculations and showed good agreement between DFT derived frequencies and the APRP surfaces. Here, we did not use DFT data but still have fairly good agreement with DFT frequencies and DFT calculated geometric parameters. This is encouraging because it would be very expensive to calculate vibrational frequencies from XMS-CASPT2 Hessians, but here we did not use either XMS-CASPT2 gradients or XMS-CASPT2 Hessians.

The optimized geometric parameters and frequencies of the N–H dissociated species also show good agreement with DFT calculations; these results are given in Sec. S2 of the supplementary material.

D. Barrier on the excited surface and minimum-energy conical intersection

The existence of a barrier on S_1 along the N–H stretch that is associated with a saddle point has been well documented in previous work.[3–7] We optimized this structure with our APRP surface and compare the resulting energies and geometrical parameters to those obtained by other methods in Table VIII. The height of our barrier is smaller than the XMS13 results and larger than the WXGY19 results, but it is in good agreement with the TLM14 calculations. All the methods show similar N–H bond distances, although again we have the best agreement with TLM14. The reported H1–N–C–H2 improper torsions are all in good agreement; the amino group was found to have a flat structure at the saddle point. All four methods have a ciscoid structure, i.e., H5 is in the same plane as the flat amino group. For all four methods, H5 is *cis* relative to the H1 around the C–N bond stretch.

The minimum-energy conical intersection (MECI) is another important structure to characterize the surfaces, although one must be cautious not to overestimate the importance of the MECI relative to the importance of the whole accessible portion of the CI seam.[56] We found the MECI geometry for our APRP surfaces using a penalty function and Broyden-Fletcher-Goldfarb-Shanno optimizer, as described in previous work.[36–38] These results, along with the MECI results from other methods, are reported in Table IX. Our MECI is a little lower in energy compared to the other methods, and our N–H1 bond length is shifted to a slightly shorter distance. The reported H1–N–C–H2 improper torsions show good agreement. The C–N–H1 bond angles are similar between the three method; these values are all close to 120°. For all three methods, the MECI

TABLE VIII. Energy difference from the optimized excited state to the saddle point and geometric parameters of the saddle point calculated for the adiabatic PES by various methods.

Method	Δ (eV)	r_{N-H1} (Å)	$\tau_{H1-N-C-H2}$ (deg)	Reference
APRP	0.37	1.39	0	This work
XMS13	0.76	1.34	0	5
TLM14	0.42	1.37	0	17
WXGY19	0.28	1.31	...	16

TABLE IX. Minimum energy conical intersection (MECI) energies and geometric parameters from different methods.

Method	MECI (eV)	r_{N-H1} (Å)	$\tau_{H1-N-C-H2}$ (deg)	θ_{C-N-H1} (deg)	Reference
APRP	4.81	1.88	3	120	This work
XMS13	5.04	1.93	0	124	5
WXGY19	4.99	1.95	...	122	16

TABLE X. Adiabatic potentials and geometric parameters of the S_0/S_1 conical intersection calculated with the APRP surface along a path with the selected θ_{C-N-H1} values with XMS-CASPT2(6,6) values at the same coordinates.

	APRP		XMS-CASPT2					
θ_{C-N-H1} (deg)	V_1 (eV)	V_2 (eV)	V_1 (eV)	V_2 (eV)	r_{N-H1} (Å)	r_{N-H2} (Å)	θ_{C-N-H2} (deg)	$\tau_{H1-N-C-H2}$ (deg)
90	5.19	5.22	5.28	5.42	1.88	0.99	124	0
100	5.09	5.10	5.12	5.30	1.88	1.00	121	0
110	4.82	4.82	4.85	4.94	1.88	1.01	111	1
120	4.81	4.81	4.75	4.95	1.88	1.01	110	3
130	4.82	4.82	4.72	4.95	1.88	1.01	110	3
140	4.85	4.85	4.75	4.96	1.88	1.01	111	4

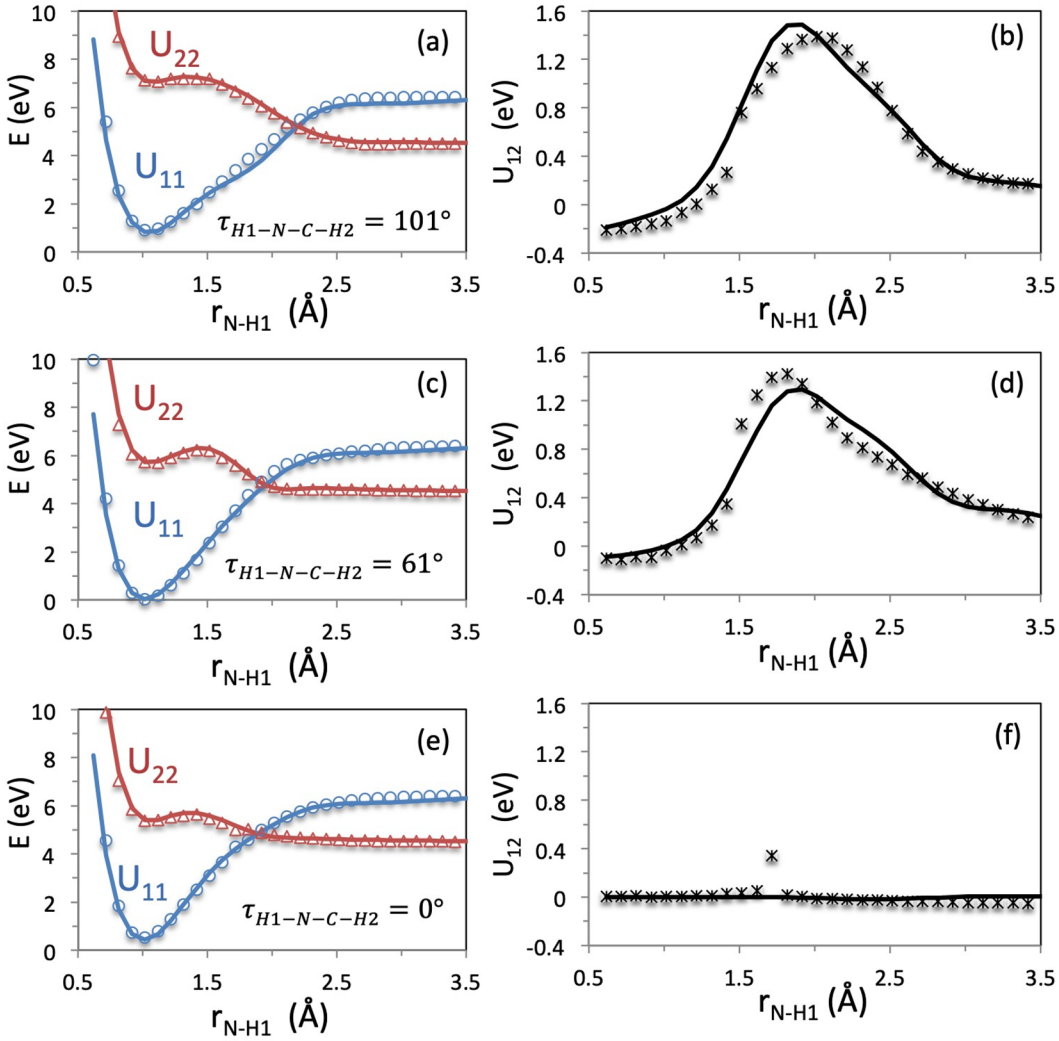

FIG. 6. Diabatic energies and diabatic couplings along primary coordinates, all slices are along the N–H1 dissociation. (a) and (b) are the diabatic energies and couplings, respectively, with the H1–N–C–H2 improper torsion at 101°; (c) and (d) are at 61°, and (e) and (f) are at 0°. The APRP results are the lines, and the XMS-CASPT(6,6) diabatic potentials and couplings are the circles, triangles, and stars.

geometries appear to be ciscoid, with H5 in plane with the amino group and *cis* to H1 around the C–N bond.

Levi and co-workers[19,20] found a conical intersection seam for methylamine by exploring the surface around a structure with N–H1 at 1.83 Å, N–H2 at 1 Å, and both C–N–HX angles around 120°. The structure was ciscoid with the amino flat. By keeping all atomic positions fixed except for H1, they found a seam along the C–N–H1 angle. We have found a similar conical intersection seam in our APRP surfaces. The energies and geometric parameters of our seam are given in Table X along with XMS-CASPT2(6,6) calculations at the same structures.

We calculated the lowest-energy conical intersection point for each fixed value of the C–N–H1 angle, and the results are given in Table X (note that V_1 is not necessarily equal to V_2 because the optimization converged before the results was identical to 0.01 eV). The resulting structures were consistently ciscoid with the amino group in a plane with H5. Most bond distances and angles are almost identical for all points on the seam, the one exception being the C–N–H2 angle. For the first two entries (C–N–H1 = 90° and 100°), the C–N–H2 angle is close to 120°. At C–N–H1 = 110° and larger bends, the C–N–H2 angle is consistently close to 110°. The XMS-CASPT2 results have a higher S_1 value, but the two states are close in energy for the entire range, showing that the adiabatic potentials resulting from diagonalizing the fitted DPEM have the conical intersection seam close to its location in direct adiabatic calculations.

E. Selected cuts and subsurfaces of the adiabatic and diabatic potentials and diabatic couplings

In this section, we show various slices of our APRP surfaces and compare the results to XMS-CASPT2(6,6) calculations at the same geometries. We discuss both diabatic potentials and adiabatic potentials.

Figure 5 shows slices through the adiabatic potentials along the primary coordinates. Panel (a) has the H1–N–C–H2 improper torsion set to 101°, panel (b) has it at 61°, and panel (c) has it at 0°. These are the three values used for our anchor points. The N–H bond distance ranges from ~0.6 Å to 3.5 Å. The APRP results show a little bumpiness but otherwise are in good agreement with the XMS-CASPT2(6,6) results. The slight bumpiness in the potential arises from the fit of the diabatic coupling rather than from bumpiness of the diabatization method.

Figure 6 shows the diabatic potentials and diabatic coupling at the same coordinates as in Fig. 5. The APRP diabatic energies are in good agreement with the data, but the diabatic coupling shows some small discrepancies. When the DPEM is diagonalized, these discrepancies cause the slight bumpiness discussed above in regard to the adiabatic energies (Fig. 5), but overall, the APRP surfaces agree well with the XMS-CASPT(6,6) results.

Figure 7 shows the APRP and XMS-CASPT(6,6) derived adiabatic potentials along the N–H1 stretch with the C–N–H2 angle at either (a) 130° or (b) 80°. The C–N–H2 coordinate is a tertiary coordinate in our APRP fit, so these slices demonstrate the tertiary contribution to the APRP fit. There is some bumpiness in our fit around r_{N-H1} = 2.5 Å, and this seems to come from some slight bumpiness in the fit of the diabatic coupling (as opposed to being produced by the diabatization method), but overall, the fit shows

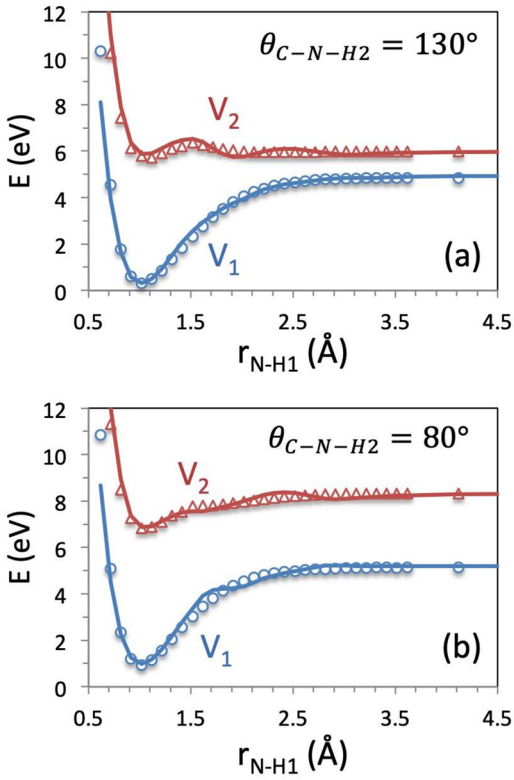

FIG. 7. Adiabatic potentials along the N–H1 dissociation with C–H–H2 at (a) 130° and (b) 80°. APRP results are the lines, and XMS-CASPT(6,6) results are the circles and triangles.

good agreement with the XMS-CASPT(6,6) data. The ground and excited surfaces are well separated at 80° and closer in energy at 130°. This difference in energy separation between the states is likely due to there being less distinction between p orbitals on the N as the bend gets larger. The good agreement between APRP and XMS-CASPT(6,6) for these data not included in our fitting procedure is very encouraging.

In Fig. 8, we show slices along two tertiary coordinates, C–N and C–H7. The results illustrate an important limitation of our surfaces, namely, that they cannot dissociate along all bond distances. While the C–H7 bond is allowed to dissociate, the C–N bond distance is not due to its functional form. As shown in Fig. 9(a), the APRP energy contribution from the C–N stretch grows rapidly around 2 Å. The N–H2 bond dissociation (not shown in this figure) is also not allowed along our surfaces, and this is an important limitation to keep in mind for future use of these DPEMs. As our surfaces are designed to model N–H1 pathways, we believe that this is an acceptable approximation.

In addition to showing this limitation, Fig. 8 also shows how our surface extrapolates between anchor points. For the calculations in this figure, the H1–N–C–H2 improper torsion was set to 30° (approximately halfway between the anchor point values of 0° and ~60°) and the N–H1 bond distance was set to 1.6 Å (approximately

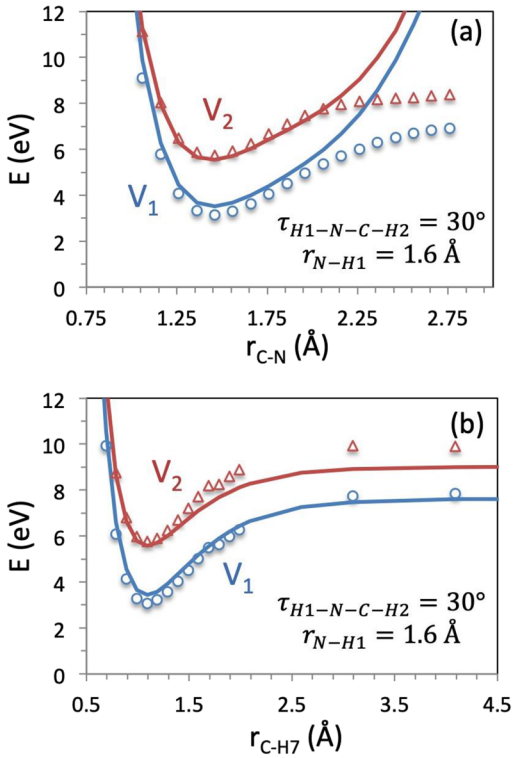

FIG. 8. Adiabatic potentials along the (a) C–N stretch and (b) C–H7 stretch with the primary coordinates parameters: N–H1 = 1.6 Å and H1–N–C–H2 = 30°. The APRP results are the lines, and XMS-CASPT(6,6) results are the circles and triangles.

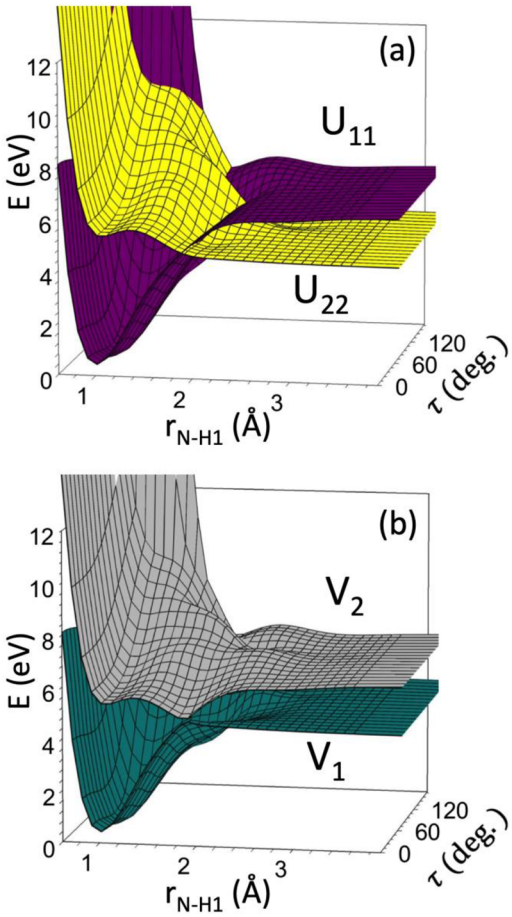

FIG. 9. 3D plots of the APRPs along the primary coordinates in the (a) diabatic and (b) adiabatic representations. The diabatic potentials are the diagonal elements of the DPEM, and the adiabatic potentials are the eigenvalues of the DPEM.

halfway between the anchor point values of ~1.0 Å and 2.2 Å). The tertiary contribution at these structures depends on the parameters at anchor points [2, 2], [2, 3], [3, 2], and [3, 3], but it is as far away as possible from these anchor point inside a square on the grid.

For both C–N and C–H7 plots, the APRP V_1 results are a slightly higher in energy compared to XMS-CASPT(6,6), and the APRP V_2 results are slightly lower. Overall, the APRP results are close to those from direct XMS-CASPT(6,6) calculations for these structures that are far from anchor points.

Figure 9 shows the three-dimensional plots of our APRP surfaces along the primary coordinates. Figure 9(a) shows the diabatic potentials, and Fig. 9(b) shows the adiabatic potentials. Trajectories can be run in either representation.

F. Suitability for trajectory calculations

To check for possible holes, we ran hundreds of trajectories with various starting conditions on S_1 and S_0; the initial conditions for some of the trajectories have considerable energy in every mode, and some of the trajectories are at high energy. The trajectories were run using the ANT program with coherent switching with decay of mixing in the adiabatic representation. These trajectories revealed no unphysical holes, confirming our expectation stated at the end of Sec. II D. Data for two sample test trajectories are presented in the supplementary material.

IV. SUMMARY

We constructed analytic diabatic potential energy matrices for the photodissociation of methylamine by using DQ diabatization and APRP fitting, with both methods being extended for the present application. For the DQ diabatization method, we incorporated a coordinate-dependent weighting scheme for the contribution of the quadrupole moments, and we showed that using this approach, we could get reasonable diabatic potentials along multiple dissociation pathways. For the APRP method, we fit data along tertiary coordinates to new kinds of functional forms, and we used a two-dimensional tent function to interpolate between the anchor points. The resulting potential energy surfaces can be used in dynamics studies of the photodissociation of the N–H bond.

SUPPLEMENTARY MATERIAL

See the supplementary material for the following two files: (1) a PDF file containing parameters for Eqs. (7)–(18) (Tables S1–S26);

geometric parameters and frequency calculations for the CH_3NH ground and excited states calculated from the APRP DPEM and by DFT; Cartesian coordinates for the following structures calculated from the APRP DPEM: the optimized ground and excited states for CH_3NH_2, and CH_3NH, the MECI, and the transition state on S_1; sample plots of energy vs time for trajectories initialized on S_1 and S_0; and (2) the Fortran routine for the potential and its gradients in the adiabatic and diabatic representations and for the nonadiabatic coupling in the adiabatic representation. The routine is also available from the online POTLIB library[47] at https://comp.chem.umn.edu/potlib/.

ACKNOWLEDGMENTS

The authors thank Chad E. Hoyer, Zoltán Varga, Siriluk Kanchanakungwankul, Linyao Zhang, Yinan Shu, and the late Steven L. Mielke for helpful discussions. We are grateful to Elliot Bernstein for helpful discussion of the experiments. This work was supported, in part, by the U.S. Department of Energy, Office of Science, Office of Basic Energy Sciences under Award No. DE-SC0015997.

DATA AVAILABILITY

The data that support the findings of this study are openly available in [the Data Repository for the University of Minnesota (DRUM)] at https://doi.org/10.13020/4f95-ex37.[57]

REFERENCES

[1] J. V. Michael and W. A. Noyes, J. Am. Chem. Soc. **85**, 1228 (1963).
[2] G. C. G. Waschewsky, D. C. Kitchen, P. W. Browning, and L. J. Butler, J. Phys. Chem. **99**, 2635 (1995).
[3] E. Kassab, J. T. Gleghorn, and E. M. Evleth, J. Am. Chem. Soc. **105**, 1746 (1983).
[4] K. M. Dunn and K. Morokuma, J. Phys. Chem. **100**, 123 (1996).
[5] H. Xiao, S. Maeda, and K. Morokuma, J. Phys. Chem. A **117**, 5757 (2013).
[6] C. L. Reed, M. Kono, and M. N. R. Ashfold, J. Chem. Soc., Faraday Trans. **92**, 4897 (1996).
[7] M. N. R. Ashfold, R. N. Dixon, M. Kono, D. H. Mordaunty, and C. L. Reed, Philos. Trans. R. Soc., A **355**, 1659 (1997).
[8] A. Golan, S. Rosenwaks, and I. Bar, Isr. J. Chem. **47**, 11 (2007).
[9] A. Golan, S. Rosenwaks, and I. Bar, J. Chem. Phys. **125**, 151103 (2006).
[10] S. J. Baek, K.-W. Choi, Y. S. Choi, and S. K. Kim, J. Chem. Phys. **117**, 10057 (2002).
[11] S. J. Baek, K.-W. Choi, Y. S. Choi, and S. K. Kim, J. Chem. Phys. **118**, 11026 (2003).
[12] M. H. Park, K.-W. Choi, S. Choi, S. K. Kim, and Y. S. Choi, J. Chem. Phys. **125**, 084311 (2006).
[13] D.-S. Ahn, J. Lee, J.-M. Choi, K.-S. Lee, S. J. Baek, K. Lee, K.-K. Baeck, and S. K. Kim, J. Chem. Phys. **128**, 224305 (2008).
[14] R. Marom, U. Zecharia, S. Rosenwaks, and I. Bar, J. Chem. Phys. **128**, 154319 (2008).
[15] M. Epshtein, A. Portnov, and I. Bar, Phys. Chem. Chem. Phys. **17**, 19607 (2015).
[16] Y. Wang, C. Xie, H. Guo, and D. R. Yarkony, J. Phys. Chem. A **123**, 5231 (2019).
[17] J. O. Thomas, K. E. Lower, and C. Murray, J. Phys. Chem. A **118**, 9844 (2014).
[18] D. P. Taylor and E. R. Bernstein, J. Chem. Phys. **103**, 10453 (1995).
[19] C. Levi, G. J. Halász, Á. Vibók, I. Bar, Y. Zeiri, R. Kosloff, and M. Baer, J. Chem. Phys. **128**, 244302 (2008).
[20] C. Levi, G. J. Halász, Á. Vibók, I. Bar, Y. Zeiri, R. Kosloff, and M. Baer, Int. J. Quantum Chem. **109**, 2482 (2009).
[21] M.-J. Hubin-Franskin, J. Delwiche, A. Giuliani, M.-P. Ska, F. Motte-Tollet, I. C. Walker, N. J. Mason, J. M. Gingell, and N. C. Jones, J. Chem. Phys. **116**, 9261 (2002).
[22] P.-F. Loos, N. Galland, and D. Jacquemin, J. Phys. Chem. Lett. **9**, 4646 (2018).
[23] T. Shiozaki, W. Győrffy, P. Celani, and H.-J. Werner, J. Chem. Phys. **135**, 081106 (2011).
[24] K. Andersson, P. A. Malmqvist, B. O. Roos, A. J. Sadlej, and K. Wolinski, J. Phys. Chem. **94**, 5483 (1990).
[25] A. A. Granovsky, J. Chem. Phys. **134**, 214113 (2011).
[26] J. C. Tully and R. K. Preston, J. Chem. Phys. **55**, 562 (1971).
[27] M. Child, in *Atom-Molecule Collision Theory*, edited by R. B. Bernstein (Plenum Press, New York, 1979), p. 427.
[28] A. W. Jasper, B. K. Kendrick, C. A. Mead, and D. G. Truhlar, in *Modern Trends in Chemical Reaction Dynamics: Experiment and Theory (Part 1)*, edited by X. Yang and K. Liu (World Scientific, Singapore, 2004), p. 329.
[29] B. C. Garrett and D. G. Truhlar, in *Theory of Scattering: Papers in Honor of Henry Eyring; Theoretical Chemistry: Advances and Perspectives*, edited by D. W. Henderson (Academic, New York, 1981), p. 215.
[30] J. B. Delos, Rev. Mod. Phys. **53**, 287 (1981).
[31] C. A. Mead and D. G. Truhlar, J. Chem. Phys. **77**, 6090 (1982).
[32] A. W. Jasper and D. G. Truhlar, in *Conical Intersections: Theory, Computation and Experiment*, edited by W. Domcke, D. R. Yarkony, and H. Köppel (World Scientific, Singapore, 2011), p. 375.
[33] C. E. Hoyer, X. Xu, D. Ma, L. Gagliardi, and D. G. Truhlar, J. Chem. Phys. **141**, 114104 (2014).
[34] C. E. Hoyer, K. Parker, L. Gagliardi, and D. G. Truhlar, J. Chem. Phys. **144**, 194101 (2016).
[35] K. R. Yang, X. Xu, and D. G. Truhlar, J. Chem. Theory Comput. **10**, 924 (2014).
[36] K. R. Yang, X. Xu, J. Zheng, and D. G. Truhlar, Chem. Sci. **5**, 4661 (2014).
[37] S. L. Li and D. G. Truhlar, J. Chem. Phys. **146**, 064301 (2017).
[38] L. Zhang, D. G. Truhlar, and S. Sun, J. Chem. Phys. **151**, 154306 (2019).
[39] H.-J. Werner, P. J. Knowles, G. Knizia, F. R. Manby, and M. Schütz, Wiley Interdiscip. Rev.: Comput. Mol. Sci **2**, 242 (2012).
[40] H.-J. Werner, P. J. Knowles, G. Knizia, F. R. Manby, M. Schütz, P. Celani, W. Györffy, D. Kats, T. Korona, R. Lindh, A. Mitrushenkov, G. Rauhut, K. R. Shamasundar, T. B. Adler, R. D. Amos, S. J. Bennie, A. Bernhardsson, A. Berning, D. L. Cooper, M. J. O. Deegan, A. J. Dobbyn, F. Eckert, E. Goll, C. Hampel, A. Hesselmann, G. Hetzer, T. Hrenar, G. Jansen, C. Köppl, S. J. R. Lee, Y. Liu, A. W. Lloyd, Q. Ma, R. A. Mata, A. J. May, S. J. McNicholas, W. Meyer, T. F. Miller III, M. E. Mura, A. Nicklass, D.P. O'Neill, P. Palmieri, D. Peng, K. Pflüger, R. Pitzer, M. Reiher, T. Shiozaki, H. Stoll, A. J. Stone, R. Tarroni, T. Thorsteinsson, M. Wang, and M. Welborn, MOLPRO, version 2019.2, a package of *ab initio* programs, https://www.molpro.net.
[41] J. D. Dill and J. A. Pople, J. Chem. Phys. **62**, 2921 (1975).
[42] W. J. Hehre, R. Ditchfield, and J. A. Pople, J. Chem. Phys. **56**, 2257 (1972).
[43] P. C. Hariharan and J. A. Pople, Mol. Phys. **27**, 209 (1974).
[44] M. S. Gordon, Chem. Phys. Lett. **76**, 163 (1980).
[45] T. Clark, J. Chandrasekhar, G. W. Spitznagel, and P. V. R. Schleyer, J. Comput. Chem. **4**, 294 (1983).
[46] B. O. Roos, Adv. Chem. Phys. **69**, 399 (1987).
[47] R. J. Duchovic, Y. L. Volobuev, G. C. Lynch, A. W. Jasper, K. R. Yang, D. G. Truhlar, T. C. Allison, A. F. Wagner, B. C. Garrett, J. Espinosa-García, and J. C. Corchado, *POTLIB, An Online Library of Potential Energy Surfaces* (University of Minnesota, Minneapolis, 2020), available at https://comp.chem.umn.edu/potlib.
[48] B. Ruscic, R. E. Pinzon, M. L. Morton, G. von Laszevski, S. J. Bittner, S. G. Nijsure, K. A. Amin, M. Minkoff, and A. F. Wagner, J. Phys. Chem. A **108**, 9979 (2004).
[49] B. Ruscic, R. E. Pinzon, G. von Laszewski, D. Kodeboyina, A. Burcat, D. Leahy, D. Montoy, and A. F. Wagner, J. Phys.: Conf. Ser. **16**, 561 (2005).
[50] J. P. Porterfield, D. H. Bross, B. Ruscic, J. H. Thorpe, T. L. Nguyen, J. H. Baraban, J. F. Stanton, J. W. Daily, and G. B. Ellison, J. Phys. Chem. A **121**, 4658 (2017).
[51] Y.-C. Chang, B. Xiong, D. H. Bross, B. Ruscic, and C. Y. Ng, Phys. Chem. Chem. Phys. **19**, 9592 (2017).

[52]B. Ruscic, Int. J. Quantum Chem. **114**, 1097 (2014).
[53]B. Ruscic, and D. H. Bross, "Active Thermochemical Tables (ATcT) values based on ver. 1.122g of the Thermochemical Network," 2019, retrieved from ATcT.anl.gov.
[54]Y. Zhao and D. G. Truhlar, Theor. Chem. Acc. **120**, 215 (2008).
[55]A. D. Boese and N. C. Handy, J. Chem. Phys. **116**, 9559 (2002).
[56]D. G. Truhlar, Faraday Discuss. **127**, 242 (2004).
[57]K. A. Parker and D. G. Truhlar (2020). "Adiabatic and diabatic energy data for the ground and first excited singlet states of CH_3NH_2," Retrieved from the Data Repository for the University of Minnesota. https://doi.org/10.13020/4f95-ex37.